Applied Catalysis B: Environmental 330 (2023) 122527

Contents lists available at ScienceDirect

Applied Catalysis B: Environmental

journal homepage: www.elsevier.com/locate/apcatb

Steering the structure and reactivity of Ag/Al_2O_3 by the addition of multi-functional WO_x for NO_x reduction by ethanol

Jungseob So [a,1], Seung Jun Lee [b,1], Minkyu Kim [b], Hyeonwoo Shin [c], Wo Bin Bae [c], Sung Bong Kang [c,*], Young Jin Kim [a,*]

[a] Environment & Sustainable Resources Research Center, Korea Research Institute of Chemical Technology, Daejeon 34114, the Republic of Korea
[b] School of Chemical Engineering, Yeungnam University, 280 Daehak-ro, Gyeongsan 38541, the Republic of Korea
[c] Research Center for Innovative Energy and Carbon Optimized Synthesis for Chemicals (Inn-ECOSysChem) and School of Earth Sciences and Environmental Engineering, Gwangju Institute of Science and Technology, 123 Cheomdan-Gwagiro, Gwangju 61005, the Republic of Korea

ARTICLE INFO

Keywords:
Ag/Al_2O_3
Tungstate
Ethanol-SCR
Lean NO_x reduction
DFT calculation

ABSTRACT

Ag/Al_2O_3 has shown promising deNO_x activity for (O)HC-SCR but has not yet been commercialized due to its narrow operating temperature range. Here, we developed AgW/Al_2O_3 exhibiting superior reactivity for ethanol-SCR compared to Ag/Al_2O_3 in the entire reaction temperature range. STEM-EDS visibly confirmed the hierarchical structure of AgW/Al_2O_3 where W was highly dispersed over Al_2O_3, and Ag species in contact with W had a narrow size distribution. UV–vis, H_2-TPR, and DRIFT results demonstrated that the abundant metallic Ag in AgW/Al_2O_3 accelerated the activation of ethanol into acetaldehyde, leading to improved NO_x conversion at low to medium temperatures, while ethylene formed over W-induced Brønsted acid sites appeared to contribute to maintaining the high-temperature deNO_x capacity. DFT calculations further supported that AgW/Al_2O_3 is more reactive toward acetaldehyde formation than Ag/Al_2O_3, and the corresponding active phases of AgW/Al_2O_3 were predicted to be predominantly metallic Ag along with Ag ionically bonded with WO_3.

1. Introduction

Growing concerns regarding global climate change have led to worldwide efforts to reduce emissions of greenhouse gases, including anthropogenic CO_2, mainly caused by the consumption of fossil fuels [1]. A rapid transition to electric vehicles (EV), which is already revolutionizing transportation sectors and their supporting infrastructure, would be a straightforward solution to mitigating CO_2 emissions. However, time is still needed for the expansion of electric vehicles, security of infrastructure, such as the linkage of the EV with the electrical grid, and finally eco-friendly generation of electricity [2]. From this point of view, lean-burn engine vehicles, which emit a relatively lower amount of CO_2 combined with greater thermodynamic efficiency than standard gasoline vehicles, would be an attractive option during the transition period toward electric vehicles [3]. However, the oxygen-rich conditions often lead to high nitrogen oxide (NO_x) emissions, which should be reduced for the sustainable application of lean-burn engines, including diesel engines [4].

Selective Catalytic Reduction of NO_x by Urea (Urea-SCR) is one of the most effective technologies applicable to NO_x reduction under oxygen-rich conditions in the transportation sector. This system has been recognized as reliable due to its high activity and durability. Furthermore, its commercial viability has been demonstrated by successful application in diesel engines to respond to the recent stricter exhaust emission regulations [5]. However, urea-SCR still has some disadvantages such as high cost, the system's complexity, and the need to periodically replenish the urea solution [6]. Moreover, incomplete urea decomposition at below 200 °C often causes malfunction of the urea-SCR system at low temperatures [6], which may require an additional technology to respond cold-start period [7]. Also, this SCR system could potentially be threatened by reactant supply chain issues, such as the shortage of urea that occurred in East Asia around the end of 2021. Because of these disadvantages of urea-SCR, many researchers have focused on alternative SCR systems utilizing non-urea (NH_3) reductants [6,8].

It has recently been demonstrated that H_2 selectively reduces NO_x in the presence of oxygen using precious metal catalysts such as Pt and Pd, and interestingly the highest conversion to N_2 often occurs between 90

* Corresponding authors.
E-mail addresses: sbkang@gist.ac.kr (S.B. Kang), yjkim03@krict.re.kr (Y.J. Kim).
[1] These authors contributed equally to this work

https://doi.org/10.1016/j.apcatb.2023.122527
Received 31 October 2022; Received in revised form 24 December 2022; Accepted 23 February 2023
Available online 24 February 2023
0926-3373/© 2023 The Authors. Published by Elsevier B.V. This is an open access article under the CC BY-NC-ND license (http://creativecommons.org/licenses/by-nc-nd/4.0/).

and 150 °C depending on supports [9]. Although the powerful NO_x reduction at low temperatures can be significantly beneficial for lean-burn operations including diesel, the narrow range of operating temperature (<200 °C) of H_2-SCR and its poor selectivity to N_2 are decisive disadvantages for commercialization [9]. From a practical point of view, the selective catalytic reduction of NO_x with CO (CO-SCR) is more desirable since vehicle exhaust generally contains CO and the concentration can be easily controlled by the engine operating conditions [9,10]. However, the operating temperature of CO-SCR should be expanded toward a high-temperature region for practical applications [9].

Another alternative technology is the selective catalytic reduction of NO_x by hydrocarbons (HC-SCR) or oxygenated hydrocarbons (OHC-SCR), where a HC or a mixture of HCs is employed as a reductant to reduce NO_x [11]. This system has a substantial advantage over other technologies because it uses onboard fuel. The most representative catalyst for HC-SCR is alumina-supported silver (Ag/Al_2O_3), which has shown considerable activity even in the presence of H_2O and SO_2 [4,8]. However, its reaction temperature range is insufficient to respond to dynamic changes in engine operations [12]. To circumvent this issue, the addition of H_2 to the feed of the HC-SCR was suggested, and this approach significantly improved the low-temperature activity of Ag/Al_2O_3 [4]. However, an onboard supply of H_2 may not be realistic, and the need for an additional tank eliminates the benefits of HC-SCR using onboard fuel as a reducing agent. Moreover, high-temperature $deNO_x$ performance cannot be secured even in the presence of H_2, despite that it is crucial in real-world driving conditions such as DPF regeneration and high speed/high load operation.

Moving our attention to catalyst modification, adding promoters onto Ag/Al_2O_3 may enhance the low-temperature $deNO_x$ performance of HC-SCR and widen its operating temperature window. For example, Ag/Al_2O_3 doped with Pt exhibited an increased NO_x reduction activity at low temperatures [13]. Successive impregnation of Ag and Au on Al_2O_3 was also reported to be beneficial for high Ag exposure on the surface, leading to better $deNO_x$ activity compared to bare Ag/Al_2O_3 [14]. However, most studies to date on bimetallic Ag-containing catalysts have focused on precious metal bases. In addition, improvements in NO_x removal activity over a wide temperature range have not yet been achieved for the promoted HC-SCR catalysts.

Here, we report the discovery of an AgW/Al_2O_3 catalyst that effectively reduces NO_x by oxygenated hydrocarbon (ethanol) over a wide temperature range. The catalytic activity of the developed AgW/Al_2O_3 was directly compared to that of conventional Ag/Al_2O_3. Various detailed characterizations were also conducted to demonstrate the superiority of AgW/Al_2O_3 compared to Ag/Al_2O_3. Finally, a computational analysis using density functional theory (DFT) further supported the experimental results and provided a detailed mechanism for the enhanced $deNO_x$ reactivity of AgW/Al_2O_3.

2. Experimental

2.1. Catalyst preparation

For AgW/Al_2O_3, the γ-Al_2O_3 (CATALOX S® Ba-200, Sasol) support was first impregnated with $(NH_4)_6H_2W_{12}O_{40}{\cdot}xH_2O$ (Sigma Aldrich) dissolved in DI water via incipient wetness method. The sample was then dried over-night in an oven at 110 °C, followed by a calcination at 550 °C for 3 h in a muffle furnace. The calcined sample underwent Ag impregnation with $AgNO_3$ (Kojima) dissolved in DI water via incipient impregnation method again. Finally, the sample were then oven-dried overnight at 110 °C and calcined at 550 °C for 5 h in a muffle furnace. The Ag/Al_2O_3 catalysts were also prepared by the incipient wetness method for impregnating Ag on γ-Al_2O_3 (CATALOX S® Ba-200, Sasol) with $AgNO_3$ (Kojima) in aqueous solution. For drying and calcination, Ag/Al_2O_3 followed the same procedure as AgW/Al_2O_3 was subject to. The AgW/Al_2O_3 and Ag/Al_2O_3 catalysts were designated as $Ag(x)W(y)/Al_2O_3$ and $Ag(x)/Al_2O_3$, where x and y in parentheses indicate the aimed content of each metal during the catalyst preparation. The actual metal loadings in $Ag(4)W(6)/Al_2O_3$ and $Ag(4)/Al_2O_3$ were determined by the ICP-AES analysis, and they were similar to the target values, as described in Table S1.

2.2. Catalyst activity tests

The catalytic activity of ethanol-SCR over AgW/Al_2O_3 and Ag/Al_2O_3 was evaluated using a packed-bed flow reactor system at a gas hourly space velocity (GHSV) of 60,000 h^{-1}. [15]. The standard feed-gas composition was 400 ppm NO, 800 ppm C_2H_5OH, 6% O_2, 2.5% H_2O, and He balance. The syringe pumps were applied to supply ethanol into the feed. The NH_3 oxidation and NH_3-SCR activities of AgW/Al_2O_3 and Ag/Al_2O_3 were measured under the feed condition containing 400 ppm NH_3, 400 ppm NO (when used), 6% O_2, 2.5% H_2O and He balance at GHSV of 60,000 h^{-1}. To investigate the effect of reductant type on $deNO_x$ activity, 800 ppm C_2H_5OH was replaced by 800 ppm CH_3CHO + 800 ppm H_2 or 800 ppm C_2H_4. To test the sulfur tolerance of each catalyst, 20 ppm of SO_2 was added to the standard feed stream at 350 °C. The sulfated catalysts were regenerated at 550 °C for 1 h with 5% O_2 and 2.5% H_2O in He balance. To determine the conversions of reactants and the formation of products, a FT-IR equipped with a 2-m gas cell (Nicolet 6700, Thermo Electron Co.) and a gas chromatograph (GC) equipped with a TCD (HP 6890 N, Agilent) were employed [15]. N_2 was directly measured by a GC equipped with a MolSieve 5 A column [15]. To measure the turnover frequency (TOF) for ethanol-SCR, a differential reactor system, where NO_x to N_2 conversion was kept below 15%, was employed to maintain the reaction in the kinetic regime. The feed composition was identical to the standard counterpart while keeping GHSV at 600,000 h^{-1}. The TOF for ethanol-SCR was calculated from the kinetic data and Ag metal dispersion, according to

$$\mathrm{TOF}\left(S^{-1}\right) = \frac{C_{NO} \bullet X_{NO} \bullet v}{\frac{ML}{MW} \bullet D} \quad (1)$$

where C_{NO} is the concentration of species NO (mol/mL), X_{NO} is the NO_x conversion to N_2 (%), v is the volumetric flow rate (mL/s), ML is the Ag content on the catalyst (g), MW is the molecular weight of Ag (107.9 g/mol), and D is the Ag metal dispersion (%) in Table 1. Apparent activation energy was calculated from the Arrhenius plot of the TOFs.

2.3. Catalyst characterizations

The pore properties of the catalysts were determined from the N_2 isotherm, measured by a volumetric adsorption apparatus at 77 K (3Flex, Micromeritics). The specific surface area was calculated by the Brunauer-Emmet-Teller (BET) equation, and the total pore volume was determined at $P/P_0 = 0.99$. Before measurements, all samples were degassed for more than 12 h at 623 K under a vacuum condition. The crystal structure of each catalyst was determined by X-ray diffraction (XRD). X-ray diffraction data were collected using a Rigaku Rotaflex with a wavelength of 1.54059 Å (Cu).

UV–vis spectra were recorded with a UV–vis spectrophotometer (Shimadzu, UV-2501PC) in the diffuse reflectance mode between 200 and 800 nm at a step of 0.5 nm with a slit width of 1 nm. $BaSO_4$ was used as a reference sample to confirm the baseline spectrum. The dispersion and particle size of Ag (Table 1) were determined via pulse O_2 chemisorption (Autochem II 2920, Micromeritics). The chemisorption procedures are as follows: 10% O_2/He flow at 200 °C for 1 h (pretreatment) → cooling to room temperature → heating to 250 °C in H_2 flow at a ramping rate of 10 °C/min and then kept for 1 h heating → purging in He flow for 1 h → cooling to 170 °C → O_2 adsorption in 10% O_2/He flow. Assuming the Ag/O_2 stoichiometric ratio of 2, the dispersion of Ag was calculated from the total amount of adsorbed O_2 during the pulse injections. Temperature-programmed reduction (TPR) by H_2 was

Table 1
Calculated values from ICP, H_2-TPR and O_2 chemisorption results.

Catalyst	Ag contents (μmol/g)[a]	Total H_2 comsumption (μmol/g)[b]	H_2 consumption (μmol/g)[c]	Total H/Ag ratio[d]	H/Ag ratio[e]	dispersion[f] (%)	Dp[f] (nm)
Ag(4)W(6)/Al_2O_3	360.6	52.2	16.2	0.29	0.09	10.1	11.6
Ag(4)/Al_2O_3	356.9	80.4	77.2	0.45	0.43	14.2	8.3

[a] Ag contents was obtained from ICP measurements.
[b] Total amount of H_2 consumed during H_2-TPR.
[c] Amount of H_2 consumed except for the chemisorbed oxygen on metallic Ag during H_2-TPR.
[d] H/Ag molar ratio calculated from total H_2 consumption.
[e] H/Ag molar ratio calculated from H_2 consumption except for the chemisorbed oxygen.
[f] The dispersion and average particle size of Ag were calculated via O_2 chemisorption.

performed using 0.2 g of catalyst sample heated at 10 °C/min in a flowing hydrogen atmosphere (5% H_2/Ar) at a flow rate of 30 mL/min.

The Raman spectra of the alumina-supported tungsten (W/Al_2O_3) catalyst was collected using a dispersive Raman spectrometer with a 532 nm excitation source (ARAMIS, Horiba Jobin Yvan). Powder specimens were used for transmission electron microscopy (TEM) and scanning transmission electron microscopy (STEM) analyses. The samples were dispersed and sonicated in ethanol and then placed onto lacey carbon films on copper grids. HAADF-STEM images were acquired with a transmission electron microscope (Titan cubed G2 60–300, Thermo Fisher Scientific) at 200 kV or 300 kV with a spherical aberration (Cs) corrector (CEOS GmbH). X-ray photoelectron spectroscopy (XPS) measurements were performed using a K-alpha (Nexsa G2, Thermo Fisher Scientific) with an automated monochromatic X-ray source, Al−Kα. The binding energies were calibrated using the C 1 s line at 284.8 eV as reference. In-situ diffuse reflectance infrared transform spectroscopy (in-situ DRIFT) experiments were conducted to identify surface species adsorbed on the catalysts using a Nicolet 6700 spectrometer equipped with a mercury cadmium telluride (MCT) detector cooled by liquid N_2 and a commercial DRIFT cell (PIKE, Diffuse IR). DRIFT data were collected in the Kubelka−Munk format with 32 scans averaged per spectrum at 4 cm^{-1}. Prior to each experiment, the catalyst sample was pretreated at 500 °C for 1 h under the flow of 6% O_2/He at 100 mL/min and then cooled to 200 °C. The catalyst was then subject to a feed of NO, C_2H_5OH, 6% O_2, and 2.5% H_2O balanced with He under a 100 mL/min flow rate with temperature varied from 200 to 500°C.

NH_3 adsorption was also investigated by in-situ DRIFT spectroscopy using NH_3 as a probe molecule. Prior to each experiment, the catalyst sample was pretreated at 300 °C for 1 h under a flow of 10% O_2 under an Ar environment. After the pretreatment, 1% NH_3/Ar was flowed into the cell for 30 min and then the cell was evacuated before the spectrum were collected. For ethanol-TPSR, an FT-IR equipped with a 2-m gas cell (Nicolet 6700, Thermo Electron Co.) was used to determine the CO and CO_2 concentrations. Prior to each experiment, the catalyst sample was pretreated at 500 °C for 1 h under a flow of 10% O_2/He at 100 mL/min and then cooled to 150 °C. The catalyst was then subject to a feed of 800 ppm C_2H_5OH, 6% O_2, and 2.5% H_2O balanced with He under a 100 mL/min flow rate for 1 h, followed by evacuation. The temperature was finally increased from 150 to 600°C at a ramping rate of 10 °C/min, while flowing 6% O_2 and 2.5% H_2O balanced with He.

2.4. Computational details

All plane-wave DFT calculations were performed using the projector augmented wave pseudopotentials provided in the Vienna ab initio simulation package (VASP) [16]. The Perdew–Burke–Ernzerhof (PBE) exchange-correlation functional with a plane wave expansion cutoff of 600 eV and 400 eV for the bulk and slab, respectively, was used. The dispersion interactions were modeled using the DFT-D3 method developed by Grimme et al. [17]. Four layers were used to model the Ag(111), Al_2O_3(100), and WO_3(001) films; the (111), (100), and (001) facets were chosen because they are thermodynamically stable [18–20]. The lateral dimensions of the slab were fixed to the PBE bulk lattice constant. Fig. 1 shows the slabs of Ag(111), Al_2O_3(100), and WO_3(001) with corresponding unit cells, and each configuration provides the potential active sites. The bottom two layers were fixed, but all other lattice atoms were allowed to relax during the calculations until the forces were less than 0.05 eV/Å. A vacuum spacing of ~ 25 Å was included, which is sufficient to reduce the periodic interaction in the surface normal direction. In terms of system size, a 2 × 2 unit cell with a corresponding 2 × 2 × 1 Monkhorst–Pack k-point mesh was used. DFT calculations were performed for a single C_2H_5OH molecule adsorbed within the 2 × 2 surface models of Ag(111), Al_2O_3(100), and WO_3(001), which correspond to a C_2H_5OH coverage of less than ~ 10 % of the total density of surface metal atoms. In the present study, the adsorption energy, E_{ads}, of an adsorbed C_2H_5OH molecule on the surface was defined using the following expression:

$$E_{ads} = \left(E_{C_2H_5OH} + E_{surf}\right) - E_{C_2H_5OH+surf} \quad (2)$$

where $E_{C_2H_5OH+surf}$ is the energy of C_2H_5OH on the bare surface; E_{surf} is the energy of the bare surface; and $E_{C_2H_5OH}$ is the energy of an isolated C_2H_5OH molecule in the gas phase. From the equation above, a large positive value for the binding energy indicates high stability of the adsorbed C_2H_5OH molecule under consideration. The barriers for C_2H_5OH dehydrogenations on the modeled surfaces were evaluated using the climbing nudged elastic band (cNEB) method [21]. All the activation energy barriers have an imaginary vibrational frequency at the transition state. The equation for binding energy was modified for the CO molecule, but the only changes were the adsorbed and gas-phase molecules.

3. Results and discussions

3.1. Catalytic activities

We compared catalytic activities of AgW/Al_2O_3 and Ag/Al_2O_3 for removing NO_x by ethanol, as presented in Fig. 2. Ag/Al_2O_3 followed the typical volcano-shape temperature-activity curves, where unselective combustion of ethanol with O_2 becomes dominant at higher temperatures, depleting reductants [4]. AgW/Al_2O_3 presented markedly higher deNO_x activity as compared to Ag/Al_2O_3 in the entire reaction temperature range. This indicates that the addition of W into Ag/Al_2O_3 is highly beneficial for accelerating selective NO_x reduction into N_2 by ethanol over a wide temperature range. Considering the significant drop of NH_3 formation in AgW/Al_2O_3 compared to Ag/Al_2O_3 at temperatures below 350 °C, high NO_x to N_2 conversion of AgW/Al_2O_3 was thought to be strongly related to lower NH_3 concentrations downstream. However, the rates of NH_3 formation at high temperatures (>450 °C) were similar in AgW/Al_2O_3 and Ag/Al_2O_3. Therefore, the capacity to maintain high reactivity of AgW/Al_2O_3 at high temperatures most likely originates from a different mechanism and this will be separately discussed. In addition, the TOFs for the ethanol-SCR reaction on AgW/Al_2O_3 and Ag/Al_2O_3 were investigated in the differential reactor (Fig. S1). AgW/Al_2O_3 showed higher TOFs and lower apparent activation energy

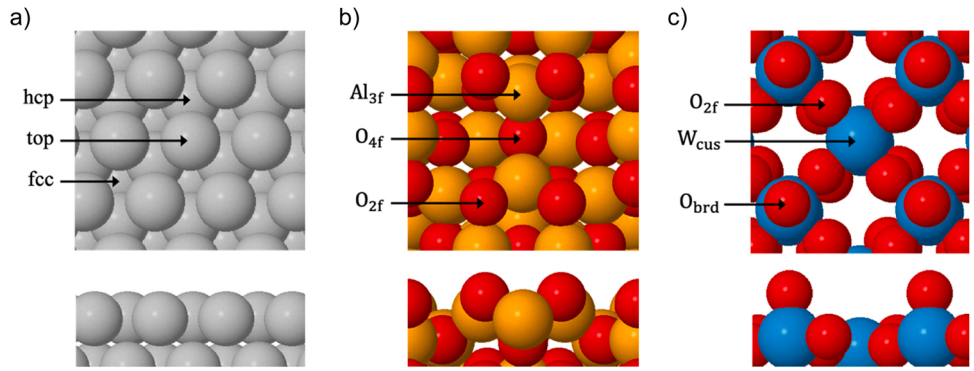

Fig. 1. Top and side views of the a) Ag(111), b) Al_2O_3(100), c) WO_3(001) surfaces. The subscripts (cus, brd, 2f, 3f, and 4f) in the figure b) and c) represent the coordinatively unsaturated site, bridge, two-fold coordinated, three-fold coordinated, and four-fold coordinated, respectively. Color scheme: Gray (Ag), Yellow (Al), Blue (W), and Red (O).

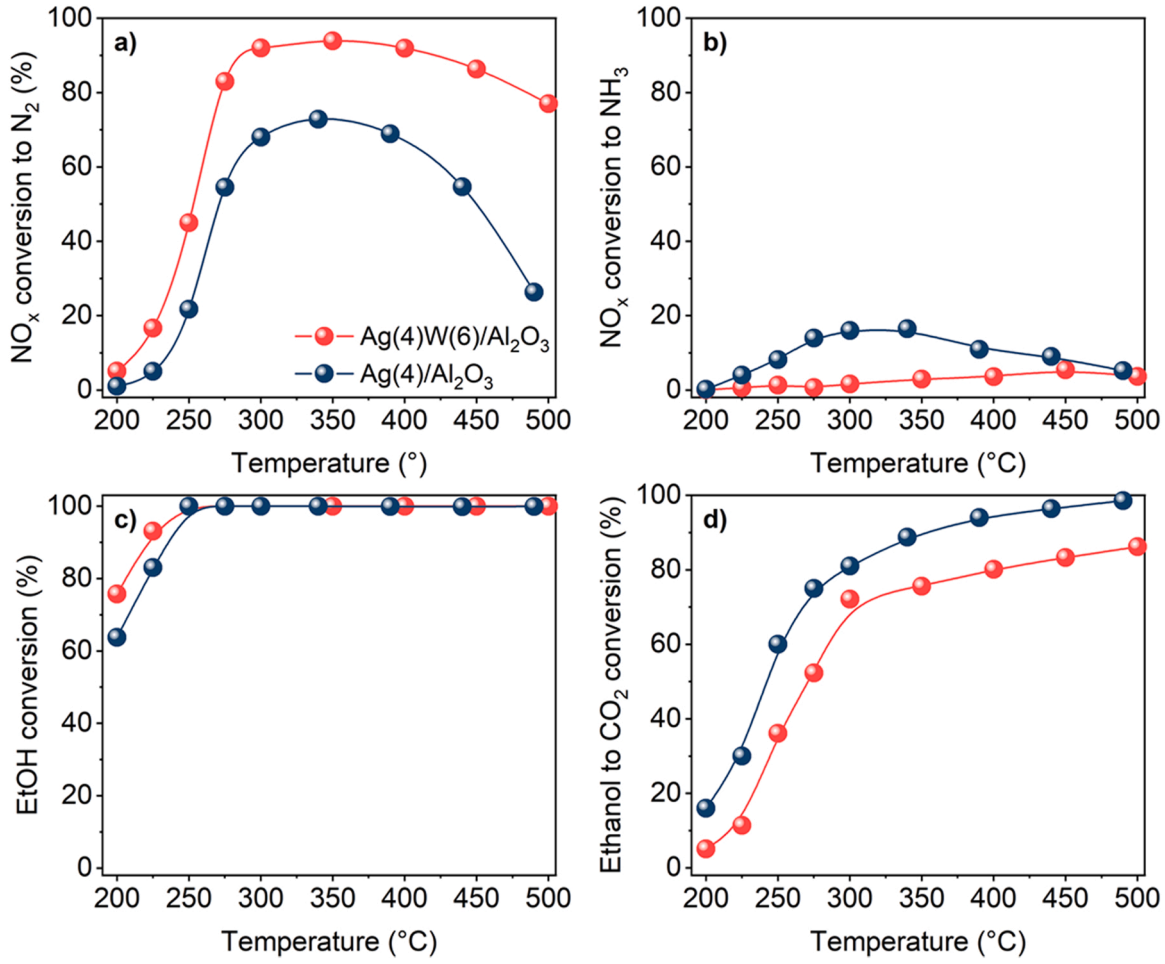

Fig. 2. Comparison of catalytic activities over AgW/Al_2O_3 and Ag/Al_2O_3 during ethanol-SCR. Feed condition: 400 ppm NO, 800 ppm C_2H_5OH, 6% O_2, 2.5% H_2O and He balance. GHSV: 60,000 h^{-1}.

(88.4 kJ/mol) than Ag/Al_2O_3 (129.0 kJ/mol), indicating the structural change in Ag species may occur upon the addition of W [12]. In addition, the amount of W in AgW/Al_2O_3 was varied for optimization, and the results clearly indicate that the W-added catalysts (AgW/Al_2O_3) exhibited far better deNO_x activity than Ag/Al_2O_3, although a small amount of W (1 wt%) in AgW/Al_2O_3 induced only a marginal increase in reactivity above 300 °C (Fig. S2a). Based on the results, the 6 wt% W-added catalyst that showed the best deNO_x activity (Fig. S2a) was used for the subsequent characterizations and discussions.

C_1/NO_x feed ratio, the ratio of the hydrocarbon feed concentration (ethanol) on the C_1 basis to NO_x feed concentration, was varied in consideration of fuel consumption during the NO_x reduction. When the C_1/NO_x feed ratio decreased from 4 to 2, Ag/Al_2O_3 exhibited a considerable drop in deNO_x activity over a wide temperature range, as seen in Fig. S2b, consistent with previous reports [15]. On the contrary, only a marginal drop was observed in the case of AgW/Al_2O in response to decreasing the C_1/NO_x feed ratio. The presence of W in AgW/Al_2O_3 not only increases the reactivity, but also appears to be beneficial for

reducing reductant consumption during NO_x conversion. Furthermore, when sulfur tolerance of AgW/Al_2O_3 was directly compared to Ag/Al_2O_3 (Fig. S3), AgW/Al_2O_3 still exhibited better performance than Ag/Al_2O_3 in the presence of 20 ppm SO_2, although the $deNO_x$ activities of both catalysts gradually decreased. It is noteworthy that the SO_2 concentration in the exhaust gas stream from the diesel engine is normally below 1 ppm due to the use of ULSD (Ultra-Low-Sulfur Diesel). The $deNO_x$ activity of AgW/Al_2O_3 was nearly recovered after the post-treatment at 550 °C for 1 h in 5% O_2 and 2.5% H_2O in He balance. Thus, the catalytic activity of AgW/Al_2O_3 was less affected by SO_2 than that of the bare Ag/Al_2O_3.

3.2. Structural characterization

Many studies have reported that the structure of Ag supported on alumina highly influences the catalytic activity in hydrocarbon or oxygenated hydrocarbon-based $deNO_x$ systems. When preparing an alumina-supported Ag catalyst, diverse Ag species including both ionic (Ag^+ and $Ag_n^{\delta+}$) and metallic Ag (Ag^0) are present on the surface in Ag/Al_2O_3, and their distribution varies with silver weight loading and the preparation method [15]. Ag/Al_2O_3 synthesized with low Ag content exclusively contains Ag^+ and the catalyst often exhibited a higher NO_x to N_2 conversion compared to metallic Ag (Ag^0) rich counterparts, since -NCO species decomposed from organo-NO_x compounds formed during the reaction preferentially bind to Ag^+ and then Ag^+-NCO subsequently converts into N_2 [22]. However, metallic Ag (Ag^0) species are also crucial in activating $deNO_x$ activity in a low-temperature region, since they can facilitate partial oxidation of hydrocarbons (HC) or oxygenated hydrocarbons, which may, in turn, lead to the formation of important surface intermediates such as enol and acetate [15,23]. Therefore, precise control of the Ag distribution in Ag/Al_2O_3 catalyst is critical to optimize the $deNO_x$ activity.

First, to investigate the origin of the enhanced reactivity of AgW/Al_2O_3, UV–visible spectroscopy and H_2-TPR were adopted to reveal the state of Ag species. In UV–visible spectroscopy, there are generally four absorption bands for Ag states, which include dispersed silver cations (Ag^+, 220 nm), partially oxidized silver clusters ($Ag_n^{\delta+}$, 260 nm), metallic Ag clusters (Ag_n^0, 290 and 350 nm), and silver nanoparticles (Ag_{NPs}, 450 nm) [24]. It should be noted that large Ag_2O particles are hard to be detected by UV–vis spectroscopy [23]. In Ag/Al_2O_3, there are a considerable amount of energy bands for dispersed silver cations and partially oxidized silver clusters (Ag^+ and $Ag_n^{\delta+}$) along with other bands for metallic Ag clusters (Ag_n^0), as seen in Fig. 3a. On the contrary, the addition of W induced a significant change in UV–vis spectra bands of the Ag species and in turn the metallic Ag clusters (290 and 350 nm) became dominant among Ag species on the surface of AgW/Al_2O_3 (Fig. 3a). TPR analysis is a characterization tool that enables us to investigate the electronic property of Ag supported on metal oxide and has been used to distinguish the state of Ag species on Al_2O_3. From low to high temperatures, we can distinguish the reduction of surface oxygen on metallic Ag (Ag_n^0), and the reductions of large Ag_2O, partially oxidized Ag clusters ($Ag_n^{\delta+}$), and Ag ions (Ag^+) [25]. Fig. 3b shows that the addition of W shifted the reduction peak of Ag species from 230 °C to 90 °C. As presented in Fig. 3b, the broad reduction peak at 230 °C indicates that Ag_2O nanoparticles and dispersed Ag^+ cations are the main species on the surface of Ag/Al_2O_3 [25]. On the contrary, a sharp reduction peak at 90 °C in AgW/Al_2O_3 is attributed to the reduction of surface oxygen on metallic Ag. It has been widely accepted that the high-temperature reduction peak is attributed to Ag strongly interacting with supports, while the low-temperature peaks below 200 °C are

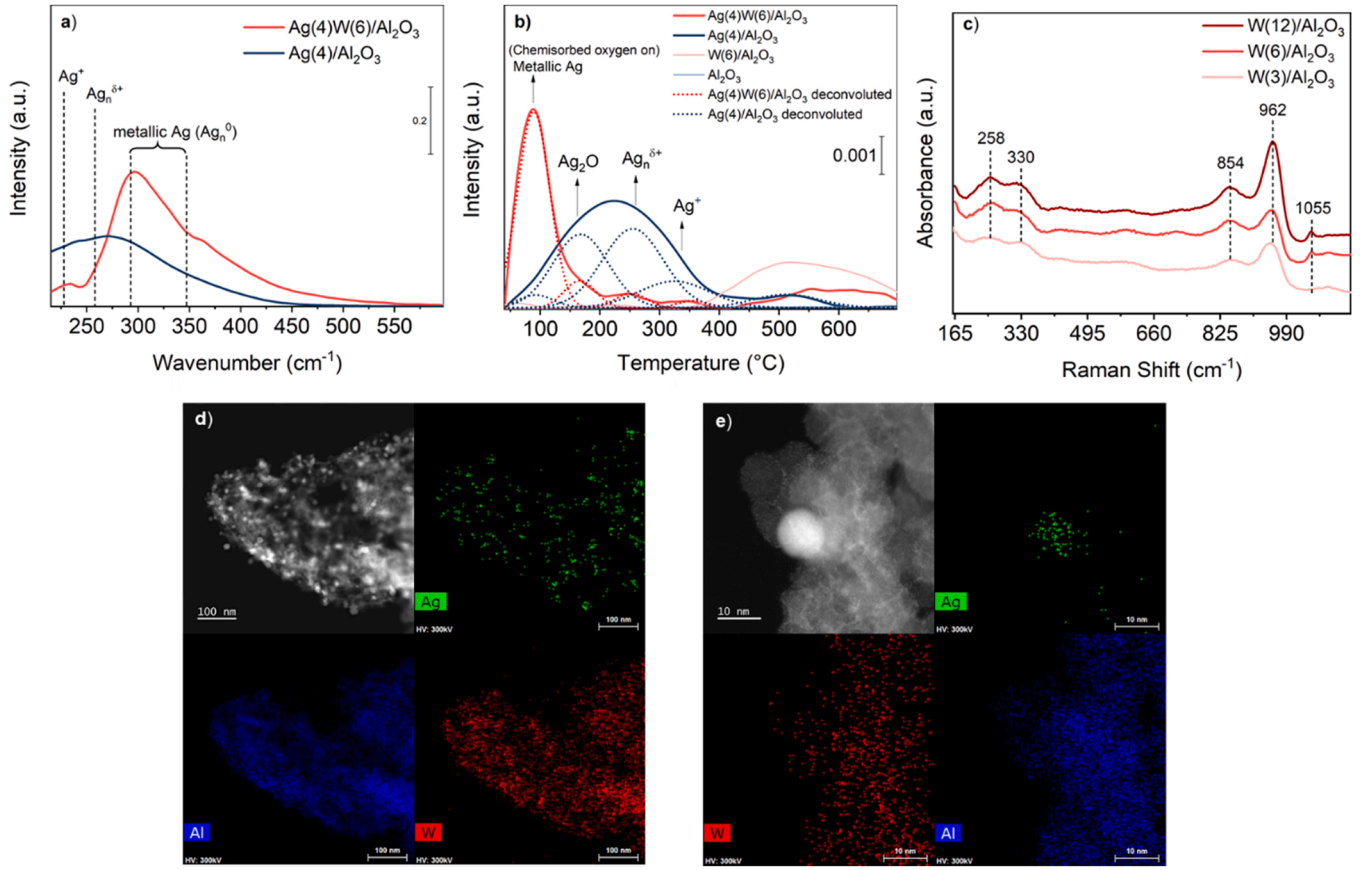

Fig. 3. a) UV–vis spectra of AgW/Al_2O_3 and Ag/Al_2O_3. b) H_2-TPR profiles AgW/Al_2O_3 and Ag/Al_2O_3. c) Raman spectra (532 nm) of AgW/Al_2O_3 and Ag/Al_2O_3. d) Low-magnification HAADF-STEM images and the corresponding EDS elemental mapping of AgW/Al_2O_3. e) High-magnification HAADF-STEM images and the corresponding EDS elemental mapping of AgW/Al_2O_3.

related to metallic Ag and Ag_2O particles [25]. Thus, the reduction peak shift toward low temperature indicates that the metal-support interaction becomes weaker upon the addition of W.

The H_2 consumption during H_2-TPR was also quantified for each catalyst to further investigate the state of Ag, as listed in Table 1. The amount of total H_2 consumption of AgW/Al_2O_3 (52.2 μmol/g) was lower than that of Ag/Al_2O_3 (80.4 μmol/g), although both catalysts have similar Ag content. The amount of H_2 consumption was also calculated except the reduction peak at around 100 °C, since it is reported to be due to the chemisorbed oxygen on metallic Ag species rather than lattice oxygen coordinated with Ag [25]. Excluding H_2 consumption by the oxygen adsorbed on the surface of metallic Ag, the difference in calculated values between both catalysts became much larger (AgW/Al_2O_3: 16.2 μmol/g, Ag/Al_2O_3: 77.2 μmol/g). This result indicates the amount of metallic Ag species in AgW/Al_2O_3 is much higher than that in Ag/Al_2O_3.

The abundant metallic Ag species in AgW/Al_2O_3 might be simply thought to have originated from the agglomeration of Ag due to decreased surface area of Al_2O_3 to anchor Ag species. However, BET surface area and pore size did not show drastic changes with W addition (Table S1). STEM images (Fig. S4) also did not reveal any noticeable agglomeration of Ag species to large Ag particle in AgW/Al_2O_3 compared to Ag/Al_2O_3. Notably, Ag/Al_2O_3 showed a wide distribution of Ag species from Ag NP (<50 nm) to partially oxidized silver clusters (<1.0 nm) (Fig. S5). However, AgW/Al_2O_3 has a narrower size distribution (Fig. S4) than Ag/Al_2O_3, in line with the UV–vis and H_2-TPR results. The average particle size of Ag in AgW/Al_2O_3 (10.8 nm) estimated from STEM was larger than Ag/Al_2O_3 (7.1 nm). From the HR-TEM image, Ag(111) plane was observed in AgW/Al_2O_3 (Fig. S6). The presence of Ag_2O and metallic Ag was also confirmed in Ag/Al_2O_3 by Ag_2O(211) and Ag(111). To determine the dispersion of Ag on each catalyst, the O_2 chemisorption has been conducted. As listed in Table 1, the dispersion of Ag on AgW/Al_2O_3 (10.1%) was apparently lower than that on Ag/Al_2O_3 (14.2%). In addition, the average size of Ag in AgW/Al_2O_3 (11.6 nm) was calculated to be higher than that in Ag/Al_2O_3 (8.3 nm), which is consistent with STEM images. As is generally recognized, higher metal dispersion with smaller particle sizes is often beneficial for achieving better catalytic reactivity. However, this was not the case for AgW/Al_2O_3 and instead the chemical state of Ag in AgW/Al_2O_3 appeared to be an influential factor to determine the deNO_x activity.

Another important aspect of AgW/Al_2O_3 is the structure of WO_x. The W phases were investigated using Raman spectroscopy, as seen in Fig. 3c. We measured the Raman spectrum of W/Al_2O_3 instead of AgW/Al_2O_3 because the presence of Ag generates emission of fluorescence that is an order of magnitude higher than Raman scattering, which may render W species invisible in the Raman spectroscopy. Since Al_2O_3 supports do not exhibit any Raman bands in the 100–1100 cm^{-1} region due to the low polarizability of light atoms and the ionic character of the Al-O [26], the Raman bands in 100 ~ 1100 cm^{-1} solely originated from the W species on the Al_2O_3 surface. For all samples, Raman bands from crystalline WO_3 NPs (805, 715, 270 cm^{-1}) were not present and the two bands observed at 854 and 962 cm^{-1} represented symmetry vibration modes of W-O-W and W═O of polymeric W species [26]. Increasing W content up to 12 wt% only increased the peak intensity of 962 cm^{-1}, which indicates that a more dispersed nanocrystalline of W was formed without the bulk crystal of WO_x. Consistent with the XRD pattern where the addition of W to Al_2O_3 did not exhibit the crystal structure of W up to 12 wt%, as seen in Fig. S7, this result demonstrates that the polymeric form of WO_x was dispersed over the Al_2O_3 support. Furthermore, STEM image and EDS mapping (Fig. 3d and e) showed that highly well-dispersed thin layers of WO_x immaculately cover the alumina surface and make intimate contact with Ag species. The layer thickness of WO_x was calculated as 0.48 monolayers for 6% W loaded in AgW/Al_2O_3 (the detailed calculation is provided in SI). In addition, the surface density of W on AgW/Al_2O_3 was calculated based on the surface area measured (Table S2), and it was much lower (1.12 W/nm^2) than the threshold value (8 W/nm^2) where crystalline WO_3 starts to appear [27]. Taking the N_2 sorption data together that the BET surface area of W/Al_2O_3 hardly decreased with the increase of W content even up to 12 wt% (Table S1), it can be concluded that W is highly dispersed on Al_2O_3. Therefore, the STEM-EDS image (Fig. 3e) clearly show that a hierarchical structure of Ag-WO_x-Al_2O_3 was formed, instead of forming separate islands of Ag and WO_x on the Al_2O_3 surface. Based on the UV–vis spectrum, H_2-TPR, and TEM images, the WO_x layer induced a different electronic property of Ag compared to the case with Ag/Al_2O_3 due to the increased metallic Ag species.

Recently, the electron-donating effect of W in metal-supported catalysts has been suggested [28]. In detail, Zhiquan et al. reported that the deposition of atomically dispersed W species on the nano-sized Pd particles exhibited an increase in the d-band center of Pd due to electron transfer from W, which leads to strong oxygen adsorption capacity and activation ability [28]. To examine the possibility of electron transfer, XPS spectroscopy was conducted to compare the oxidation state of the WO_x layer in AgW/Al_2O_3 with W/Al_2O_3 (Fig. S8). However, there was no noticeable shift in the binding energy of $4f_{7/2}$ of W in AgW/Al_2O_3 compared to W/Al_2O_3. Indeed, the average size of Ag species in AgW/Al_2O_3 was relatively large for considering effective electron transfer between the metal and support [29]. At best even though transfer took place, electron donation from W to Ag could have not been observed in XPS, possibly due to the high electron density of Ag particle with 5 ~ 10 nm [29]. The abundant metallic Ag species on AgW/Al_2O_3 may not mainly originate from the electron donor-acceptor system between W and Ag.

Kwak et al., reported that unsaturated pentacoordinate Al^{3+} (Al^{3+}_{penta}) centers on the Al_2O_3 surface are anchoring sites for Pt to involve metal support interaction via an oxygen bridge [30]. On the other hand, Wang et al. reported that terminal hydroxyls on Al_2O_3 are responsible for anchoring Ag species, leading to the formation of an Ag-O-Al nano--structure [31]. Although we were not able to clearly locate the specific anchoring sites for Ag, it may be reasonably speculated that the presence of W obscured the possible anchoring sites for Ag to the Al_2O_3 surface. In the DRIFT spectra of Ag/Al_2O_3 (Fig. S9), three peaks were observed at 3770, 3730, and 3680 cm^{-1}, corresponding to hydroxyl groups on Al sites with various geometries type I, II, and III, respectively [32], which might be the primary cause for a variety type of Ag species in Ag/Al_2O_3 (Ag^+, $Ag_n^{\delta+}$, and Ag^0) due to different bonding environments. On the contrary, AgW/Al_2O_3 had reduced peak intensity for hydroxyl groups to Al sites, with an additional peak at 3656 cm^{-1}, which can be attributed to W-OH. Taking the well-dispersed WO_x layer on Al_2O_3 into account together (Fig. 3c-e), it is plausible that the consumption of strong anchoring sites on Al_2O_3 by W led to a lack of small-sized Ag species (Ag^+ and $Ag_n^{\delta+}$) other than metallic Ag species. Based on the narrow size distribution of Ag species in AgW/Al_2O_3, we speculate that the bonding environment on the WO_x layer was not as diverse as in the case of bare Al_2O_3.

3.3. Reaction pathway

As reported in previous studies [33], the ethanol-SCR is initiated with the activation of ethanol on the catalyst surface and metallic Ag has been reported to facilitate the formation of partially oxidized surface species such as acetaldehyde at low temperatures. As described in Fig. 4a, ethanol oxidation without NO_x clearly showed that significantly more acetaldehyde formed in AgW/Al_2O_3 than in Ag/Al_2O_3. This strongly indicates that metallic Ag was beneficial for activating ethanol, especially at low temperatures below 350 °C. Indeed, it was reported that as the metallic Ag concentration increases, the rate of ethanol dehydrogenation to acetaldehyde increases, which leads to increased NO_x to N_2 conversion at a low to medium temperature range [34]. Indeed, a controlled experiment over Ag/Al_2O_3 in consideration of ethanol dehydrogenation ($C_2H_5OH \rightarrow C_2H_4O + H_2$) revealed that the

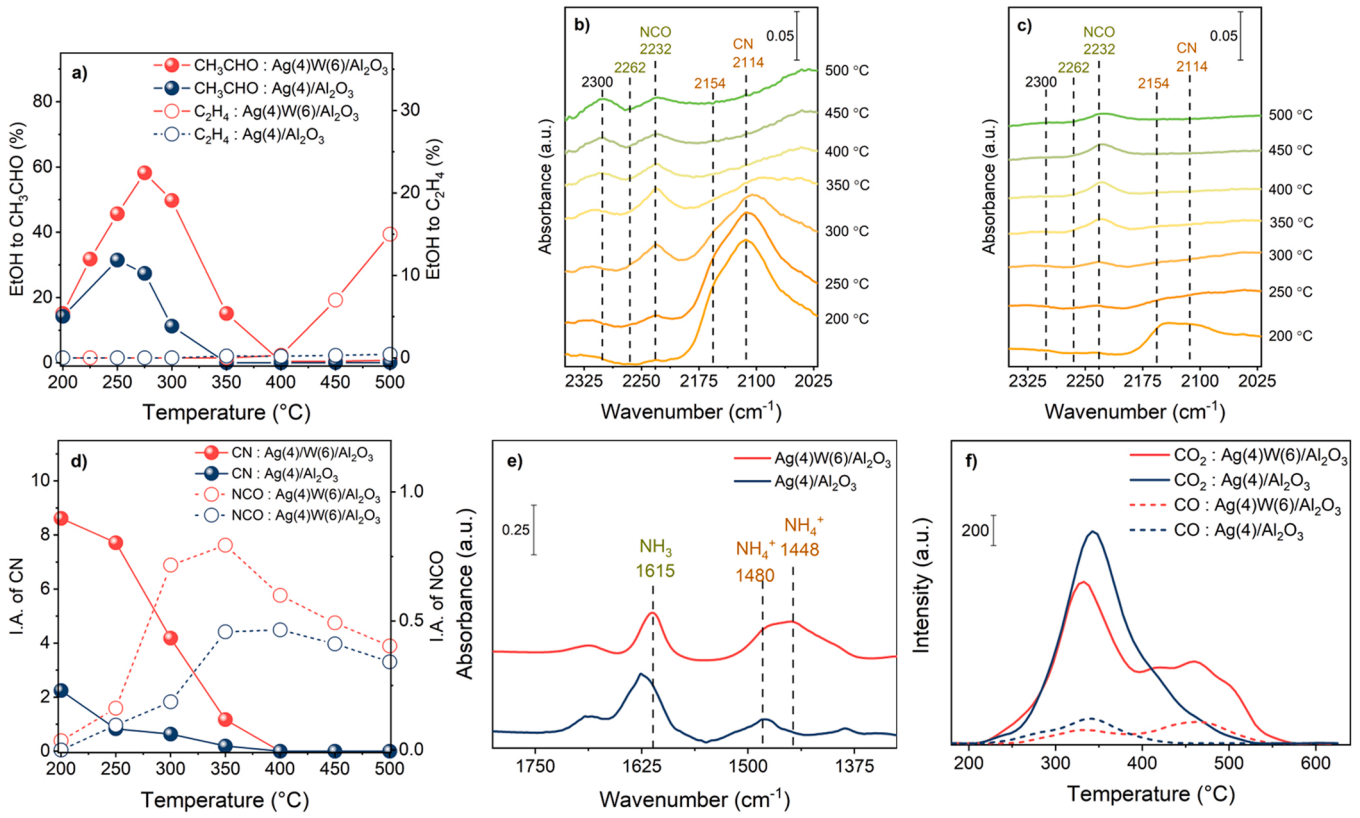

Fig. 4. a) Ethanol oxidation in the absence of NO_x over AgW/Al_2O_3 and Ag/Al_2O_3. Feed conditions: 800 ppm C_2H_5OH, 6% O_2, 2.5% H_2O, and He balance. GHSV: 60,000 h^{-1} b) and c) DRIFTS spectra of surface species on AgW/Al_2O_3 and Ag/Al_2O_3 at differet temperatures. Feed conditions: 400 ppm NO, 800 ppm C_2H_5OH, 6% O_2, and 2.5% H_2O balanced with Ar under 100 mL/min flow rate and temperature varied 200–500 °C. d) The integrated areas of -CN and -NCO peaks on AgW/Al_2O_3 and Ag/Al_2O_3 at varied temperatures. e) DRIFTS spectra of NH_3 adsorption at 40 °C. f) Ethanol-TPSR profiles over AgW/Al_2O_3 and Ag/Al_2O_3. Adsorption conditions: 800 ppm C_2H_5OH, 6% O_2, 2.5% H_2O, and He balance 150 °C for 1 h.

low-temperature $deNO_x$ activity was apparently enhanced when feeding acetaldehyde with hydrogen instead of ethanol (Fig. S10), pointing to the importance of the ethanol dehydrogenation step for achieving better $deNO_x$ performance. It is generally accepted that following the initial activation, the adsorbed oxygenated hydrocarbons ($C_xH_yO_z$) including acetaldehyde and enol further transform into organo-NO_x compounds (R-NO, R-ONO, R-NO_2) via interaction with NO and O_2 or nitrate on the catalyst surface. These organo-NO_x compounds are easily converted into cyanate and isocyanate, and then -NCO further reacts with NO to form N_2 ($NO + NCO \rightarrow CO_2 + N_2$) [4,8]. In this regard, many studies reported that -NCO derived from NO_x and ethanol is the main intermediate for producing N_2 and CO_2 in ethanol-SCR systems [4,8]. Taking this into consideration, an in-situ DRIFT study was conducted for Ag/Al_2O_3 and AgW/Al_2O_3 to investigate the evolution of surface species with varying temperatures (Fig. 4b and c). When ethanol was flowed together with NO and O_2 into the cell containing AgW/Al_2O_3 or Ag/Al_2O_3, we located both cyanide (Ag-CN and Al_2O_3-CN) at 2114 and 2154, and isocyanate (Ag-NCO and Al-NCO) vibration peaks at 2232 and 2262 cm^{-1}. The intensity of -NCO peaks continuously increased and reached the maximum at 350 °C and then decreased, thus following a similar trend as observed in the typical volcano-shape of activity curves of silver-containing $deNO_x$ catalysts (Fig. 2a). This supports the previous argument that -NCO surface species is the most relevant surface species immediately before N_2 formation [4]. -NCO peak intensity in the spectrum of AgW/Al_2O_3 remained higher than that in Ag/Al_2O_3 up to 500 °C, which indicates that the better $deNO_x$ activity of AgW/Al_2O_3 is likely related to the higher concentration of -NCO surface species over a wide temperature range.

The most pronounced difference in DRIFT spectra between the two catalysts is a noticeably higher intensity of the -CN vibrational peak in AgW/Al_2O_3. Furthermore, in contrast to the trend of -NCO species, prominent -CN vibrational peak intensities continuously decreased until 350 °C in response to an increase in temperature, consequently disappearing after 400 °C (Fig. 4d). This indicates that -CN plays another important role in the $deNO_x$ reactivity at a low and medium temperature ranges. However, there has been little study on the role of –CN, and consequently the detailed mechanism including -CN has remained elusive due to the complex reaction network. Bion et al. suggested a mechanism of ethanol-SCR based on in-situ FTIR spectroscopy, which observed that an intermittent ethanol pulse under NO and O_2 initially produced -CN formed on the Ag active sites, and then the -CN transformed into -NCO, which hydrolyzes into ammonia to further react with NO to form N_2 [35]. Starzyk et al. further presented a more detailed mechanism regarding the role of -CN and -NCO over Ag/Al_2O_3 using nanosecond time-resolved in situ spectroscopy [36]. First, -CN prefers Ag sites over Al sites, where nitrogen atoms can preferentially bind on the basis of hard-soft acid-base theory, and the formed -CN on the Ag sites flips onto Al sites via forming bridged cyanide to form –NCO. In accordance with the previous studies, we can postulate that the surface –CN works as a reservoir that continuously supplied –NCO precursors to nearby Ag/Al sites, and in turn, significantly denser surface -CN on AgW/Al_2O_3 led to higher $deNO_x$ activity, as observed in Fig. 2. It appears that the -NCO vibrational intensity increased at the expense of -CN surface species, especially at low temperatures below 350 °C, as seen in Fig. 4d, which indicates that -CN is a precursor to -NCO. On the contrary, some studies showed that -CN and -NCO followed parallel independent reaction pathways and each further reacted to form N_2 in a separate way [37]. However, in either scenario, it is obvious that a denser concentration of -CN species contributed to the powerful $deNO_x$ process of AgW/Al_2O_3 when comparing DRIFT studies with the activity results. We

also obtained transient DRIFT results over AgW/Al_2O_3 at 300 °C, where reaction intermediates are most abundant on the catalyst surface. We could observe the gradual consumption of -NCO and –CN after ethanol was cut off during the in-situ DRIFTS study (Fig. S11). This result indicates that those species play an important role as reaction intermediates rather than spectators in ethanol-SCR.

Based on a previous study which reported that acetaldehyde is easily converted to organo-NO_x compounds (R-NO, R-ONO, R-NO_2) followed by subsequent conversion into -CN and -NCO species[4], the higher formation of acetaldehyde in AgW/Al_2O_3 observed in Fig. 4a is highly likely to be related with either -NCO or -CN species concentration. Indeed, the formation of acetaldehyde was limited to a temperature of 350 °C (Fig. 4a), which coincidently overlapped with the temperature region where -CN species were clearly observed and their concentrations on the surface of AgW/Al_2O_3 remained higher than on Ag/Al_2O_3 (Fig. 4d). Therefore, it is reasonable to attribute the noticeably higher concentration of -CN in AgW/Al_2O_3 to the increased formation of acetaldehyde by ethanol dehydrogenation on the metallic Ag species.

In the medium temperature range, NH_3 slip over AgW/Al_2O_3 was significantly less than over Ag/Al_2O_3, especially as shown in Fig. 2b. Since NH_3 is one of the main byproducts of ethanol-SCR, the low NH_3 slip of AgW/Al_2O_3 is extremely advantageous for achieving high N_2 selectivity. NH_3 formed during the (HC+OHC)-SCR reaction may further react with O_2 (NH_3 oxidation) to produce N_2. Kim et al. reported the addition of AlF_3 to Ag/Al_2O_3 increased the number of acidic sites, resulting in a significant improvement in NO_x to N_2 conversion by facilitating in-situ oxidation of NH_3 into N_2 on the catalyst surface [38]. Employing a systematical approach, a dual-bed reactor consisting of Ag/Al_2O_3 catalyst in the front bed and CuZSM5 catalyst in the rear bed was employed for successive NH_3 oxidation, resulting in improvement of NO_x to N_2 conversion [15]. However, Fig. S12 shows that the NH_3 oxidation activity over AgW/Al_2O_3 is substantially inferior compared to the unpromoted counterpart. In addition, the NH_3-SCR reaction between NH_3 and NO_x turned out to be trivial for both Ag/Al_2O_3 and AgW/Al_2O_3 (Fig. S13). Therefore, the reaction path of NO_x to NH_3 was most likely suppressed by W addition. Indeed, Obuchi et al. revealed that NH_3 formation decomposed from organo-nitrile N-oxides species mostly on the Al_2O_3 surface [39]. Therefore, the limited exposure of Al_2O_3 to the W layer in AgW/Al_2O_3 might be a reason for low NH_3 slip compared to $AgAl_2O_3$.

Another attractive advantage of AgW/Al_2O_3 is that its NO_x reduction capability is maintained at high temperatures, which is highly beneficial for high-speed/high load conditions and/or DPF regeneration [40]. Metallic Ag species are generally believed to be responsible for the combustion of hydrocarbon or oxygenated hydrocarbon at high temperatures, adversely affecting NO_x conversion [4,41]. Surprisingly, AgW/Al_2O_3 mainly containing metallic Ag species exhibited only a marginal drop in deNO_x activity even at high temperatures in contrast to Ag/Al_2O_3. More acetaldehyde formation caused by metallic Ag cannot solely explain the high-temperature deNO_x of AgW/Al_2O_3 since acetaldehyde formation was limited above 400 °C. Interestingly, as depicted in Fig. 4a, ethylene was produced via ethanol oxidation only from AgW/Al_2O_3 above 400 °C, and not from Ag/Al_2O_3. Indeed, ethanol can be transformed into ethylene via dehydration over solid catalysts [42], and this reaction is known to occur on both Brønsted acid and Lewis acid sites, the rate of which depends on the type of acid sites [42]. This ethanol dehydration may be closely related to the improved NO_x to N_2 conversion over AgW/Al_2O_3, as will be discussed later.

To determine the surface acidic property, a DRIFT study was performed over both catalysts using NH_3 as probe molecules. NH_3 adsorption produced several kinds of NH_3-derived surface species, as presented in Fig. 4e. The vibration peak at 1615 cm^{-1} is due to the deformation vibration of NH_3 coordinated to Lewis acid sites, while the other peak at 1480 cm^{-1} corresponds to the deformation vibration of NH_4^+ adsorbed on Brønsted acid sites [43]. Indeed, the number of Brønsted acid sites is reported to significantly increase when WO_x is supported on metal oxides including Al_2O_3, TiO_2, and ZrO_2 [44]. Consistent with the previous study, AgW/Al_2O_3 revealed a significantly higher amount of NH_4^+ associated with Brønsted acid sites, compared to the case with bare Ag/Al_2O_3. In addition, the broad peak of $\delta_{N-H,asym}$ bending modes of NH_4^+ for AgW/Al_2O_3 indicates the presence of Brønsted acid sites with diverse acidic strength on the surface [43]. Compared with the NH_3 adsorption spectrum of Ag/Al_2O_3, it appears that stronger Brønsted acid sites were generated on the surface of WO_3 in AgW/Al_2O_3, since additional bending modes ($\delta_{N-H,asym}$) of NH_4^+ was red-shifted. The protons (H^+) on Brønsted acid sites are known to catalyze dehydration reactions [42,45]. Some studies on ethanol dehydration into ethylene over diverse types of W oxides have been reported [42,45]. Li et at. reported that WO_3 nanowire rich in oxygen vacancies was highly selective for ethylene formation from ethanol during photocatalysis [45]. Recently, Vlachos et al. also reported that W layers deposited on Pt form Brønsted acid sites, leading to the facile formation of propylene from propanol via dehydration [42]. Combining the current results with previous studies, we can conclude that the presence of Brønsted acid sites in AgW/Al_2O_3 activated ethanol dehydration to ethylene at high temperatures above 400 °C, possibly by the elevated reaction temperature, which is beneficial for the deNO_x process. Indeed, the light-off of NO_x reduction by hydrocarbon typically shifts to higher temperatures compared to the case with an oxygenated counterpart, due to difficult activation. For example, ethylene-SCR over Ag/Al_2O_3 started to be active above 400 °C for NO_x conversion [46]. In addition, the light-off temperature (T_{50}) for NO_x conversion via propylene SCR is reported to be close to 380 °C [47]. As show in Fig. S10, the high-temperature SCR activity of Ag/Al_2O_3 was improved when ethanol was replaced by ethylene (NO_x conversion at 500 °C: 80%). Therefore, the excellent NO_x conversion of AgW/Al_2O_3 at elevated temperatures can be attributed to NO_x reduction by sequentially formed ethylene instead of acetaldehyde.

Based upon the experimental results (Figs. 3a, b, and 4a), W-induced metallic Ag species appeared to accelerate the ethanol conversion into acetaldehyde, which is crucial for improving the NO_x reduction reactivity at low temperature, while Brønsted acid sites in WO_x play a role in alleviating the parasitic oxidation of reductants at high temperatures via ethanol dehydration to ethylene. However, there may also be Ag-WO_3 interfacial sites, although the actual number would be much smaller than that of the monometallic sites given the large particle size of the Ag species. A computational analysis has thus been performed using DFT calculation to understand the role of interfacial sites, and to further ensure our experimental data are reliable, as will be described in the following section.

3.4. Computational results

3.4.1. Stability of adsorbed C_2H_5OH

UV–vis spectroscopy and H_2-TPR experimental results showed that the Ag ionic phase in the reference catalyst of Ag/Al_2O_3 is dominantly present compared to the Ag metallic phase (a dominant phase in AgW/Al_2O_3) shown in Fig. 2. The ionic Ag feature corresponds to the electronically unsaturated state by the electron transfer to adjacent oxygen. To model such system, we replaced a surface Al atom of Al_2O_3(100) with an Ag atom resulting in the formation of Ag-O-Al (Ag-Al_2O_3). To confirm the electronic states of Ag in Ag-Al_2O_3(100), the density of states (DOS) was additionally evaluated (Fig. S15). The simulation results clearly show the unoccupied states above the fermi level which is resulted from the electron abstractions by adjacent oxygen. In terms of AgW/Al_2O_3, Ag (111) was used to model metallic Ag phase in AgW/Al_2O_3, and the DOS simulation of Ag(111) reveals the electron rich phase compared to Ag-Al_2O_3(100) (Fig. S15). Thus, we believe that the main characteristics of Ag in Ag/Al_2O_3 and AgW/Al_2O_3 catalysts may be similar to Ag-Al_2O_3(100) and Ag(111), respectively. WO_3(001) was employed to represent WO_3 on Al_2O_3. Additionally, to consider the interfacial sites, a surface W atom in WO_3(001) was replaced with an Ag atom (Ag-WO_3). W-Ag was also selected in the same manner, while a surface Ag atom in

Ag (111) was substituted with a W atom. In summary, Ag-Al_2O_3(100) were used to model the Ag/Al_2O_3 catalyst, and the other surfaces of Ag (111), W-Ag(111), WO_3(001) and Ag-WO_3(001) were selected to model the AgW/Al_2O_3 catalyst. We computationally focused on the kinetic mechanism of acetaldehyde formation from C_2H_5OH on the model surfaces representing the Ag/Al_2O_3 and AgW/Al_2O_3 catalysts, because the formation rate of acetaldehyde is experimentally distinguishable on both catalysts. Specifically, higher acetaldehyde conversion on AgW/Al_2O_3 than on Ag/Al_2O_3 had been observed, which is correlated with higher NO_x conversion on AgW/Al_2O_3. Prior to investigating the mechanism, the stability of C_2H_5OH on the surfaces was explored by evaluating the adsorption energies. It should be noted that on metallic surfaces of Ag and W-Ag, two surface oxygens are present with adsorbed C_2H_5OH because the adsorbed oxygens would subsequently abstract the hydrogens from C_2H_5OH to produce acetaldehyde (CH_3CHO). Hydrogen transfer from C_2H_5OH to metal (oxygen not involved dehydrogenation) was also evaluated but was predicted to be kinetically and thermodynamically hindered (not shown).

Fig. 5a-e provide the energetically most favorable configurations of C_2H_5OH adsorbed on Ag/Al_2O_3 (Ag-Al_2O_3) and AgW/Al_2O_3 (Ag, W-Ag, WO_3 and Ag-WO_3) with the corresponding adsorption energies. We also tested other configurations, including C_2H_5OH on other sites and other orientations; however, those configurations were predicted to be less favorable than the most favorable configuration shown in Fig. 5a-e. The simulation predicts that C_2H_5OH strongly binds on Ag-Al_2O_3 with adsorption energy of 81.4 kJ/mol. Similar strong bindings of other carbon species having a similar number of carbons such as C_2H_6 and C_3H_6 was reported on PdO, RuO_2, and IrO_2 [48]. The strong binding of alkanes is driven by the formation of strong sigma bonding between hydrogen and surface metal atoms. However, such interactions between C_2H_5OH and Ag-Al_2O_3 were not predicted, indicating that the high stability does not stem from the formation of a sigma complex. The hydrogens of carbon (C-H) and oxygen (O-H) do not directly or strongly interact with the metal atoms of Ag or Al, but oxygen of C_2H_5OH was predicted to directly interact with substituted Ag atom (see Fig. 5a). The interactions between oxygen of C_2H_5OH and Ag trigger the high stability of Ag-Al_2O_3.

On the AgW/Al_2O_3 catalyst, we also found a similar binding mechanism of strong interactions between O and metal atom, and this leads to high stability of adsorbed C_2H_5OH (Ag: 91.4 kJ/mol, WO_3: 156 kJ/mol and Ag-WO_3: 81.1 kJ/mol), as seen in Fig. 5a-e. On the W substituted Ag surface, we found that the O-H bond was dissociated, and C_2H_5O and OH were formed during the DFT relaxation, meaning that C_2H_5OH is unstable when adjacent oxygen is present. More specifically, the oxygen of

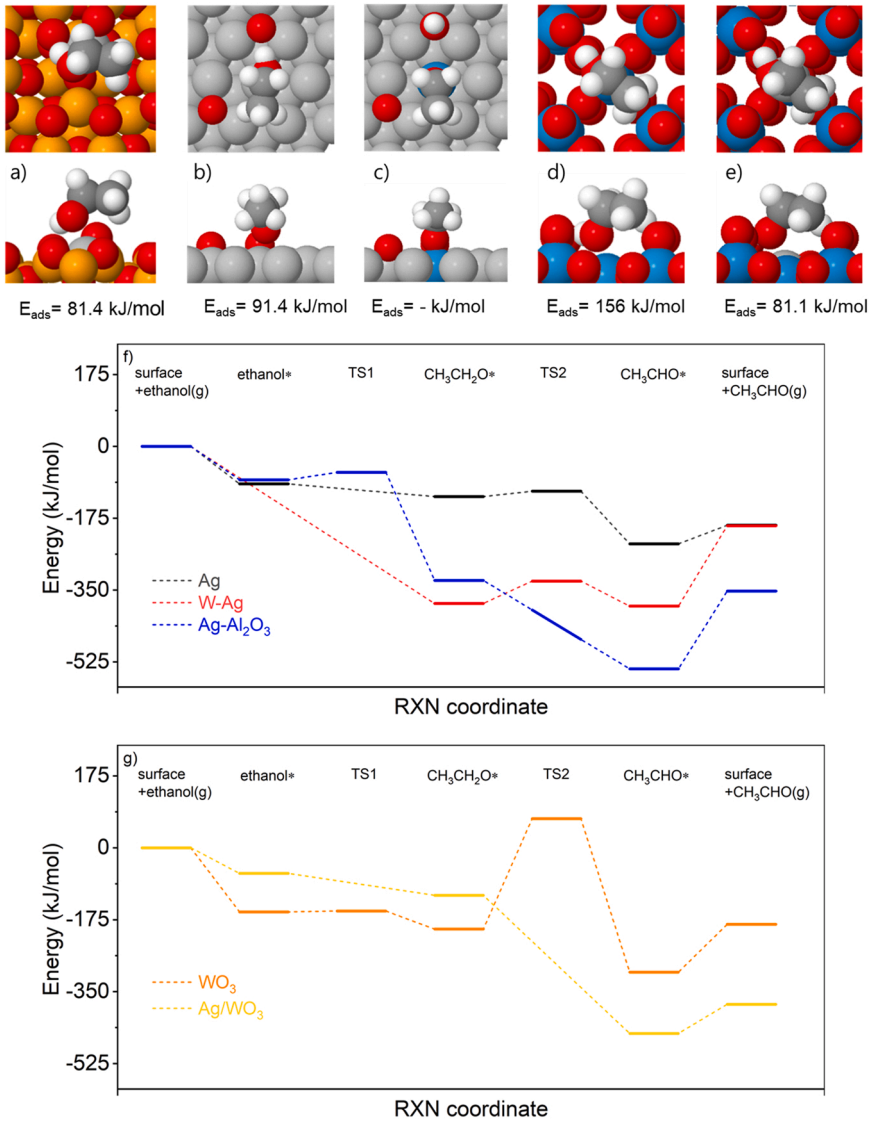

Fig. 5. DFT predicted favored configurations of C_2H_5OH on a) Ag-Al_2O_3, b) Ag, c) W-Ag, and d) WO_3, e) Ag-WO_3. Energy diagrams of acetaldehyde formation from C_2H_5OH on f) Ag, W-Ag, Ag-Al_2O_3, g) WO_3, and Ag-WO_3.

C_2H_5OH strongly undergoes back-donation interactions with substituted W; the electron transfer from occupied states of W to unoccupied states of oxygen. The back-donation interactions would fill the antibonding states of O-H bond, resulting in weakening of this bond. Therefore, O-H bond cleavage simultaneously occurs when C_2H_5OH adsorbs on the W-Ag surface. From the perspective of kinetics, the dissociative adsorption of C_2H_5OH on W-Ag is expected.

3.4.2. Kinetics of Acetaldehyde Formation from C_2H_5OH

With the predicted stable configurations shown in Fig. 5a-e, we evaluated the kinetics of acetaldehyde formation from C_2H_5OH. The dehydrogenation of C_2H_5OH occurs through reactions with the adjacent oxygens, and O-H bond cleavage was predicted to be more facile compared to C-H bond cleavage on the surfaces [49]. Thus, we focused on the following sequence of dehydrogenation: 1) $C_2H_5OH + O \rightarrow C_2H_5O + OH$, and 2) $C_2H_5O + O \rightarrow$ acetaldehyde + OH. Fig. 5f shows the energy diagrams of dehydrogenation kinetics from C_2H_5OH to acetaldehyde. Our simulations predict that the reactions on all surfaces show strong exothermicity. On the reference catalyst of Ag-Al_2O_3, the O-H bond cleavage was predicted to be thermodynamically and kinetically facile; the reaction needs to overcome the small energy barrier of 18 kJ/mol ($\Delta E = -245$ kJ/mol), and the subsequent C-H bond cleavage generating acetaldehyde is barrier-less kinetics ($\Delta E = -215$ kJ/mol). These simulation results suggest that the Ag/Al_2O_3 catalyst readily produces adsorbed acetaldehyde due to the favorable kinetics and thermodynamics; however, adsorbed acetaldehyde binds excessively strongly on the surface to desorb from the surface ($E_{ads} = 189$ kJ/mol). The predicted high stability of acetaldehyde corresponds closely to the experimentally observed low conversion (desorption rate) of acetaldehyde from Ag/Al_2O_3.

On the W-Ag surface of the AgW/Al_2O_3 catalyst, similar behavior had been predicted, indicating facile dehydrogenation with strong binding of acetaldehyde ($E_{ads} = 196$ kJ/mol). The W-Ag surface actively generates adsorbed acetaldehyde, but the surface does not allow acetaldehyde to desorb from the surface. Because of the predicted same kinetic behaviors of Ag-Al_2O_3 and W-Ag, an identical role can be expected. However, other factors such as site blocking by other carbon species (intermediates) potentially affect the reactivity of both surfaces having similar kinetic behaviors of acetaldehyde formation. To verify the potential of site blocking, the stability of CO (partially oxidized from ethanol) was evaluated on Ag-Al_2O_3 and W-Ag surfaces. The simulation predicts that CO strongly binds on the W site of the W-Ag surface while CO on the Ag site of Ag-Al_2O_3 has low stability (282 kJ/mol vs. 30.2 kJ/mol). The results suggest that as CO forms on the W-Ag catalytic surface, the highly stable adsorbed CO triggers site blocking, thereby hindering C_2H_5OH adsorption, while it would not occur on Ag-Al_2O_3. In other words, W-Ag is active towards acetaldehyde formation, but the active sites tend to be poisoned, thereby deactivating the W-Ag phase. In contrast to the Ag-Al_2O_3 and W-Ag phases, the Ag metallic phase of the AgW/Al_2O_3 catalyst provides facile dehydrogenation kinetics and weaker acetaldehyde adsorption energy ($E_{ads} = 45.4$ kJ/mol), suggesting that the Ag metallic phase is attributed to the high conversion of acetaldehyde of AgW/Al_2O_3. Therefore, it was computationally confirmed that the Ag metallic phase plays a critical role in the high C_2H_5OH conversion of the AgW/Al_2O_3 catalyst.

WO_3 provides different dehydrogenation kinetics compared to Ag, W-Ag, and Ag-Al_2O_3 phases. The initial bond (O-H) cleavage is facile, but the subsequent C-H bond cleavage is kinetically hindered by the large energy barrier of 268.5 kJ/mol. The results suggest that the role of WO_3 would lower the acetaldehyde conversion. However, when introducing Ag atoms on the WO_3 surface (Ag-WO_3), the acetaldehyde formation becomes much more facile compared to the pristine WO_3 surface. More specifically, the initial bond (O-H) and subsequent bond cleavages do not require kinetic barriers (negligible barrier) with strong overall exothermicity ($\Delta E = -451.8$ kJ/mol). Finally, the generated acetaldehyde weakly binds on the surface ($E_{ads} = 71.1$ kJ/mol), resulting in high conversion of acetaldehyde. Such kinetic behavior on Ag-WO_3 is similar with the Ag metallic phase. Therefore, it can be concluded that the experimentally observed high conversion of acetaldehyde of AgW/Al_2O_3 catalyst is attributable to active phases of Ag-WO_3 and metallic Ag.

3.4.3. Stabilities of -CN and -NCO

In the in-situ DRIFTS study (Fig. 4b and c), key reaction intermediates, -CN and –NCO, were observed on each catalyst. AgW/Al_2O_3 reveals higher peak intensities for –CN and -NCO than Ag/Al_2O_3, which is believed to be the primary cause for the better deNO_x activity of AgW/Al_2O_3. To fundamentally support DRIFTS results, the stabilities of -CN and -NCO on the Ag surface (metallic Ag phase in AgW/Al_2O_3), Ag-WO_3 surface (Ag-WO_3 interfacial site in AgW/Al_2O_3) and Ag-Al_2O_3 surface (ionic Ag phase in Ag/Al_2O_3) were evaluated by calculating the adsorption energies. We did not focus on the absolute values of adsorption energies because of unstable gas phase levels [CN(g) and CNO(g)] resulting in the too large adsorption energies. The adsorption energies and corresponding favored configurations are shown in Fig. S16. Our simulation predict that -CN and -NCO most stably adsorb on the Ag/Al_2O_3 catalyst, and their stability was predicted to be lower on the AgW/Al_2O_3 catalyst (Ag-Al_2O_3 > Ag > Ag-WO_3). By comparing DRIFT data, the computational results show the opposite trend for -CN and -NCO. These inconsistent results suggest that the population of -CN and -NCO on both catalysts (observed in DRIFTS) may not depend on their adsorption stabilities, but on the rate of key reaction steps such as ethanol hydrogenation. To fundamentally confirm the reaction mechanism from ethanol to -CN and -NCO, further in-depth calculation analysis is needed, but it is required to explore too many possibilities for reaction pathways, which has been hardly established for ethanol-SCR to the best of our knowledge. Therefore, we think that such fundamental analysis is beyond the scope of this paper.

4. Conclusion

In this work, we presented the promotional effect of W on the NO_x reduction over Ag/Al_2O_3 by ethanol. AgW/Al_2O_3 revealed strongly superior NO_x to N_2 conversion compared to the conventional Ag/Al_2O_3 in the entire reaction temperature range. This became more pronounced when the C_1/NO_x feed ratio was decreased, which is advantageous in terms of fuel economy. In detail, TEM-EDS and Raman data confirmed the hierarchical structure of AgW/Al_2O_3, where W was highly dispersed over Al_2O_3, and Ag species was placed on the top of W. Based on STEM images and O_2 chemisorption data, the average size of Ag in AgW/Al_2O_3 appeared to be higher than that in Ag/Al_2O_3, indicating the dispersion/particle size of Ag may not be primary factors determining NO_x removal activity. UV–vis, H_2-TPR, and DRIFT results indicated that the addition of W enhanced the metallic characteristics of Ag species, resulting in facile ethanol activation into acetaldehyde, followed by -CN and -NCO formation, which is crucial for improving the NO_x reduction reactivity at low temperatures. Second, the reaction pathway of NO_x to NH_3 was likely to be depressed on Al_2O_3-covered with W, leading to increased NO_x to N_2 selectivity compared to Ag/Al_2O_3 at moderate temperatures. Finally, an NH_3-assisted DRIFT study revealed that dispersed W imparted a significant amount of Brønsted acid sites, facilitating ethanol dehydration to ethylene. The formation of ethylene was believed to be responsible for the excellent performance of AgW/Al_2O_3 above 400 °C by suppressing the parasitic oxidation of reductants, as evidenced by ethanol-TPSR. DFT calculations evaluated the stability of adsorbed C_2H_5OH and the kinetics of acetaldehyde formation on Ag/Al_2O_3 and AgW/Al_2O_3. The simulations predicted that C_2H_5OH strongly binds, and it undergoes facile initial (O-H) and subsequent (C-H) bond cleavages on both catalysts except for the WO_3 phase. Ag-WO_3 and metallic Ag, in which phases can be present in AgW/Al_2O_3, provided weaker stability of adsorbed acetaldehyde. These results fundamentally confirmed that AgW/Al_2O_3 is more active toward acetaldehyde conversion than Ag/

Al_2O_3. Furthermore, the metallic Ag along with Ag ionically bonded with WO_3 was found to be corresponding active phases for high conversion of acetaldehyde from AgW/Al_2O_3.

CRediT authorship contribution statement

J. So: Data curation, Formal analysis, Investigation, Writing – original draft. **S. J. Lee:** Data curation, Formal analysis, DFT calculation, Writing – original draft. **M. Kim:** numerical calculation, Writing – review & editing. **H. Shin:** Data curation, Formal analysis. **W. B. Bae:** Data curation, Formal analysis. **S. B. Kang:** Conceptualization, Funding acquisition, Formal analysis, Writing – review & editing. **Y. J. Kim:** Conceptualization, Funding acquisition, Supervision, Writing – review & editing.

Declaration of Competing Interest

The authors declare that they have no known competing financial interests or personal relationships that could have appeared to influence the work reported in this paper.

Data availability

Data will be made available on request.

Acknowledgements

This work was supported by Institutional Research Program of KIST (2E32370-23-P014,"Atmospheric Environment Research Program") and the Technology Development Program to Solve Climate Changes through the National Research Foundation of Korea (NRF) funded by the Ministry of Science, ICT (NRF-2019M1A2A2103855). This research was also supported by National Research Foundation of Korea (NRF) Grant funded by the Korean government (MSIT) (No. 2021R1C1C1005404 & 2021R1A5A1028138). Finally, M. Kim thanks support from National Research Foundation of Korea (NRF) under the framework of Priority Research Centers Program funded by the Ministry of Education (2014R1A6A1031189).

Appendix A. Supporting information

Supplementary data associated with this article can be found in the online version at doi:10.1016/j.apcatb.2023.122527.

References

[1] B. Fais, N. Sabio, N. Strachan, The critical role of the industrial sector in reaching long-term emission reduction, energy efficiency and renewable targets, Appl. Energy 162 (2016) 699–712.
[2] S. Brown, D. Pyke, P. Steenhof, Electric vehicles: the role and importance of standards in an emerging market, Energy Policy 38 (2010) 3797–3806.
[3] S. Schemme, R.C. Samsun, R. Peters, D. Stolten, Power-to-fuel as a key to sustainable transport systems – an analysis of diesel fuels produced from CO_2 and renewable electricity, Fuel 205 (2017) 198–221.
[4] R. Burch, J.P. Breen, F.C. Meunier, A review of the selective reduction of NOx with hydrocarbons under lean-burn conditions with non-zeolitic oxide and platinum group metal catalysts, Appl. Catal. B Environ. 39 (2002) 283–303.
[5] G. Busca, L. Lietti, G. Ramis, F. Berti, Chemical and mechanistic aspects of the selective catalytic reduction of NOx by ammonia over oxide catalysts: a review, Appl. Catal. B Environ. 18 (1998) 1–36.
[6] I.A. Resitoglu, A. Keskin, Hydrogen applications in selective catalytic reduction of NOx emissions from diesel engines, Int. J. Hydrog. Energy 42 (2017) 23389–23394.
[7] T. Ryu, J. Jeong, S.W. Byun, S. Kweon, J. Park, W.B. Bae, D.Y. Kim, Y.J. Kim, M. B. Park, S.B. Kang, Ethylene trapping of palladium-impregnated zeolites for cold-start emission control, Chem. Eng. J. 442 (2022), 136197.
[8] H. He, Y. Yu, Selective catalytic reduction of NOx over Ag/Al_2O_3 catalyst: from reaction mechanism to diesel engine test, Catal. Today 100 (2005) 37–47.
[9] H. Hamada, M. Haneda, A review of selective catalytic reduction of nitrogen oxides with hydrogen and carbon monoxide, Appl. Catal. A Gen. 421–422 (2012) 1–13.
[10] Y.-W. You, Y.J. Kim, J.H. Lee, M.W. Arshad, S.K. Kim, S.M. Kim, H. Lee, L. T. Thompson, I. Heo, Unraveling the origin of extraordinary lean NOx reduction by CO over Ir-Ru bimetallic catalyst at low temperature, Appl. Catal. B Environ. 280 (2021), 119374.
[11] C.K. Lambert, Current state of the art and future needs for automotive exhaust catalysis, Nat. Catal. 2 (2019) 554–557.
[12] J.P. Breen, R. Burch, A review of the effect of the addition of hydrogen in the selective catalytic reduction of NOx with hydrocarbons on silver catalysts, Top. Catal. 39 (2006) 53–58.
[13] F. Gunnarsson, H. Kannisto, M. Skoglundh, H. Härelind, Improved low-temperature activity of silver–alumina for lean NOx reduction – Effects of Ag loading and low-level Pt doping, Appl. Catal. B Environ. 152–153 (2014) 218–225.
[14] P.M. More, D.L. Nguyen, M.K. Dongare, S.B. Umbarkar, N. Nuns, J.S. Girardon, C. Dujardin, C. Lancelot, A.S. Mamede, P. Granger, Rational preparation of Ag and Au bimetallic catalysts for the hydrocarbon-SCR of NOx: sequential deposition vs. coprecipitation method, Appl. Catal. B Environ. 162 (2015) 11–20.
[15] M.K. Kim, P.S. Kim, J.H. Baik, I.-S. Nam, B.K. Cho, S.H. Oh, DeNOx performance of Ag/Al_2O_3 catalyst using simulated diesel fuel–ethanol mixture as reductant, Appl. Catal. B Environ. 105 (2011) 1–14.
[16] P.E. Blochl, Projector augmented-wave method, Phys. Rev. B Condens Matter 50 (1994) 17953–17979.
[17] J.P. Perdew, K. Burke, M. Ernzerhof, Generalized gradient approximation made simple, Phys. Rev. Lett. 77 (1996) 3865–3868.
[18] S.D. Kevan, R.H. Gaylord, High-resolution photoemission study of the electronic structure of the noble-metal (111) surfaces, Phys. Rev. B Condens. Matter 36 (1987) 5809–5818.
[19] M. Digne, P. Sautet, P. Raybaud, P. Euzen, H. Toulhoat, HydroxyL Groups on γ-alumina surfaces: a DFT study, J. Catal. 211 (2002) 1–5.
[20] I.N. Yakovkin, M. Gutowski, Driving force for the WO_3 (001) surface relaxation, Surf. Sci. 601 (2007) 1481–1488.
[21] G. Henkelman, B.P. Uberuaga, H. Jónsson, A climbing image nudged elastic band method for finding saddle points and minimum energy paths, J. Chem. Phys. 113 (2000) 9901–9904.
[22] K.-i Shimizu, J. Shibata, H. Yoshida, A. Satsuma, T. Hattori, Silver-alumina catalysts for selective reduction of NO by higher hydrocarbons: structure of active sites and reaction mechanism, Appl. Catal. B Environ. 30 (2001) 151–162.
[23] K.A. Bethke, H.H. Kung, Supported Ag catalysts for the lean reduction of NO with C_3H_6, J. Catal. 172 (1997) 93–102.
[24] D.Y. Yoon, J.-H. Park, H.-C. Kang, P.S. Kim, I.-S. Nam, G.K. Yeo, J.K. Kil, M.-S. Cha, DeNOx performance of Ag/Al_2O_3 catalyst by n-dodecane: effect of calcination temperature, Appl. Catal. B Environ. 101 (2011) 275–282.
[25] F. Wang, J. Ma, G. He, M. Chen, C. Zhang, H. He, Nanosize effect of Al_2O_3 in Ag/Al_2O_3 catalyst for the selective catalytic oxidation of ammonia, ACS Catal. 8 (2018) 2670–2682.
[26] E.I. Ross-Medgaarden, I.E. Wachs, Structural determination of bulk and surface tungsten oxides with UV−vis diffuse reflectance spectroscopy and Raman spectroscopy, J. Phys. Chem. C 111 (2007) 15089–15099.
[27] I. Ro, J. Qi, S. Lee, M. Xu, X. Yan, Z. Xie, G. Zakem, A. Morales, J.G. Chen, X. Pan, D.G. Vlachos, S. Caratzoulas, P. Christopher, Bifunctional hydroformylation on heterogeneous Rh-WOx pair site catalysts, Nature 609 (2022) 287–292.
[28] Z. Hou, L. Dai, J. Deng, G. Zhao, L. Jing, Y. Wang, X. Yu, R. Gao, X. Tian, H. Dai, D. Wang, Y. Liu, Electronically engineering water resistance in methane combustion with an atomically dispersed tungsten on PdO catalyst, Angew. Chem. Int Ed. Engl. 61 (2022), e202201655.
[29] Y. Lykhach, S.M. Kozlov, T. Skála, A. Tovt, V. Stetsovych, N. Tsud, F. Dvořák, V. Johánek, A. Neitzel, J. Mysliveček, S. Fabris, V. Matolín, K.M. Neyman, J. Libuda, Counting electrons on supported nanoparticles, Nat. Mater. 15 (2016) 284–288.
[30] J.H. Kwak, J. Hu, D. Mei, C.W. Yi, D.H. Kim, C.H. Peden, L.F. Allard, J. Szanyi, Coordinatively unsaturated Al^{3+} centers as binding sites for active catalyst phases of platinum on γ-Al_2O_3, Science 325 (2009) 1670–1673.
[31] F. Wang, J. Ma, S. Xin, Q. Wang, J. Xu, C. Zhang, H. He, X. Cheng, Zeng, Resolving the puzzle of single-atom silver dispersion on nanosized γ-Al_2O_3 surface for high catalytic performance, Nat. Commun. 11 (2020) 529.
[32] H. Knözinger, P. Ratnasamy, Catalytic aluminas: surface models and characterization of surface sites, Catal. Rev. 17 (1978) 31–70.
[33] Y.H. Yeom, M. Li, W.M.H. Sachtler, E. Weitz, A study of the mechanism for NOx reduction with ethanol on γ-alumina supported silver, J. Catal. 238 (2006) 100–110.
[34] A. Flura, F. Can, X. Courtois, S. Royer, D. Duprez, High-surface-area zinc aluminate supported silver catalysts for low-temperature SCR of NO with ethanol, Appl. Catal. B Environ. 126 (2012) 275–289.
[35] N. Bion, J. Saussey, M. Haneda, M. Daturi, Study by in situ FTIR spectroscopy of the SCR of NOx by ethanol on Ag/Al_2O_3—Evidence of the role of isocyanate species, J. Catal. 217 (2003) 47–58.
[36] F. Thibault-Starzyk, E. Seguin, S. Thomas, M. Daturi, H. Arnolds, D.A. King, Real-time infrared detection of cyanide flip on silver-alumina NOx removal catalyst, Science 324 (2009) 1048–1051.
[37] S. Tamm, H.H. Ingelsten, A.E.C. Palmqvist, On the different roles of isocyanate and cyanide species in propene-SCR over silver/alumina, J. Catal. 255 (2008) 304–312.
[38] P.S. Kim, B.K. Cho, I.-S. Nam, J.W. Choung, Bifunctional Ag-based catalyst for NOx reduction with E-diesel fuel, ChemCatChem 6 (2014) 1570–1574.
[39] A. Obuchi, C. Wögerbauer, R. Köppel, A. Baiker, Reactivity of nitrogen containing organic intermediates in the selective catalytic reduction of NOx with organic compounds: a model study with tert-butyl substituted nitrogen compounds, Appl. Catal. B Environ. 19 (1998) 9–22.

[40] Y.J. Kim, P.S. Kim, C.H. Kim, Deactivation mechanism of Cu/Zeolite SCR catalyst under high-temperature rich operation condition, Appl. Catal. A Gen. 569 (2019) 175–180.
[41] F.C. Meunier, J.P. Breen, V. Zuzaniuk, M. Olsson, J.R.H. Ross, Mechanistic aspects of the selective reduction of NO by propene over alumina and silver–alumina catalysts, J. Catal. 187 (1999) 493–505.
[42] J. Fu, S. Liu, W. Zheng, R. Huang, C. Wang, A. Lawal, K. Alexopoulos, S. Liu, Y. Wang, K. Yu, J.A. Boscoboinik, Y. Liu, X. Liu, A.I. Frenkel, O.A. Abdelrahman, R. J. Gorte, S. Caratzoulas, D.G. Vlachos, Modulating the dynamics of Brønsted acid sites on PtWOx inverse catalyst, Nat. Catal. 5 (2022) 144–153.
[43] S.A. Skarlis, D. Berthout, A. Nicolle, C. Dujardin, P. Granger, I.R. Spectroscopy, Analysis and kinetic modeling study for NH_3 adsorption and desorption on H- and Fe-BEA catalysts, J. Phys. Chem. C 117 (2013) 7154–7169.
[44] Ad Gutiérrez-Alejandre, P. Castillo, J. Ramírez, G. Ramis, G. Busca, Redox and acid reactivity of wolframyl centers on oxide carriers: Brønsted, Lewis and redox sites, Appl. Catal. A Gen. 216 (2001) 181–194.
[45] J. Li, G. Chen, J. Yan, B. Huang, H. Cheng, Z. Lou, B. Li, Solar-driven plasmonic tungsten oxides as catalyst enhancing ethanol dehydration for highly selective ethylene production, Appl. Catal. B Environ. 264 (2020), 118517.
[46] H. Härelind, F. Gunnarsson, S.M.S. Vaghefi, M. Skoglundh, P.-A. Carlsson, Influence of the carbon–carbon bond order and silver loading on the formation of surface species and gas phase oxidation products in absence and presence of NOx over silver-alumina catalysts, ACS Catal. 2 (2012) 1615–1623.
[47] S. Chansai, R. Burch, C. Hardacre, J. Breen, F. Meunier, Investigating the mechanism of the H_2-assisted selective catalytic reduction (SCR) of NOx with octane using fast cycling transient in situ DRIFTS-MS analysis, J. Catal. 276 (2010) 49–55.
[48] R. Martin, M. Kim, A. Asthagiri, J.F. Weaver, Alkane activation and oxidation on late-transition-metal oxides: challenges and opportunities, ACS Catal. 11 (2021) 4682–4703.
[49] Y. Choi, P. Liu, Understanding of ethanol decomposition on Rh(111) from density functional theory and kinetic Monte Carlo simulations, Catal. Today 165 (2011) 64–70.